

3D Seismic Response of the Deep Basement Structure of the Granada Basin (Southern Spain)

by S. Alejandro Gil-Zepeda, Francisco Luzón, Jorge Aguirre, José Morales,
Francisco J. Sánchez-Sesma, and Carlos Ortiz-Alemán

Abstract The Granada Basin is located in the southeast of Spain, in the central sector of the Betic Cordilleras, in an area of high seismic hazard in the Iberian Peninsula. This hazard is due, in part, to local ground-motion amplification effects that have been observed at various locations in this basin. In this work, we use the indirect boundary element method (IBEM) to compute the three-dimensional (3D) seismic response of the deep structure of the Granada Basin for incident P - and S -plane waves coming from the south. We have analyzed the results in both frequency and time domains, and for the range of frequencies that we have been able to compute (between 0 and 0.312 Hz), the most relevant site effects are the local amplifications produced inside the sediments. Generally speaking, the observed amplification patterns of the displacements for incident SH waves are the highest at those locations where the basin is deeper. For P and SV waves, the “snapshots” show the amplification effects of both radial and vertical components, when the direct waves cross the Granada Basin. The amplification levels, with respect to the amplitude of the incident wave, are not so large, because the impedance contrast between the sediments and the bedrock (equal to 2.45) is relatively low. Moreover, two perpendicular receiver profiles are used to analyze the wave propagation, and we have observed the propagation of phases that can be identified as surface waves along the two profiles. The Rayleigh waves propagate with more energy on the forward direction (from south to north) of the incident body wave.

Introduction

Local effects due to geological site conditions can lead to significant spatial and temporal variations of seismic ground motion, which can contribute to large structural damage during moderate to large earthquakes. Local site response has received significant attention in the past two decades, and its characterization has been performed by using both experimental and numerical analysis techniques (see, e.g., Aki, 1988, and Sánchez-Sesma, 1996). In recent years, numerical codes have been developed to deal with the seismic wave propagation in three-dimensional (3D) models (see e.g., Sánchez-Sesma and Luzón, 1995). The most realistic simulations to date are those of finite differences. In particular, 3D geometries have been considered for some sedimentary basins around the world: Olsen and Archuleta (1996) and Olsen (2000) used finite differences to simulate the ground motion in the Los Angeles Basin; Olsen *et al.* (1995) studied the propagation of P waves in the Salt Lake Basin; and recently, Frankel and Stephenson (2000) computed the ground motions in the Seattle region with the finite-difference method. In these and other works that used

3D realistic structures, some common phenomena, such as the generation of surface waves and localized resonances, have been observed. However, amplification patterns are generally different and are not quantitatively “portable” from one basin to another. The seismic response of each 3D basin has its own amplification levels and its own wave-motion response inside and outside the sediments. The response depends strongly on the properties of the basin, such as impedance contrast, wave velocities, and geometry of the structure. Of course, the location of the source and its rupture parameters also have significant influence in the response.

In this work, we study the seismic response of the deep structure of the Granada Basin (Fig. 1), which is located in one of the regions with the highest hazard level in the Iberian Peninsula, as shown in the Spanish seismic building code (Norma de Construcción Sismoresistente NCSE-94, 1995). Available historical records indicate that in the last 2000 years, different parts of the south of the Iberian Peninsula have been affected by major earthquakes with MSK intensities from VII to X (Reicherter, 2001). From recent history,

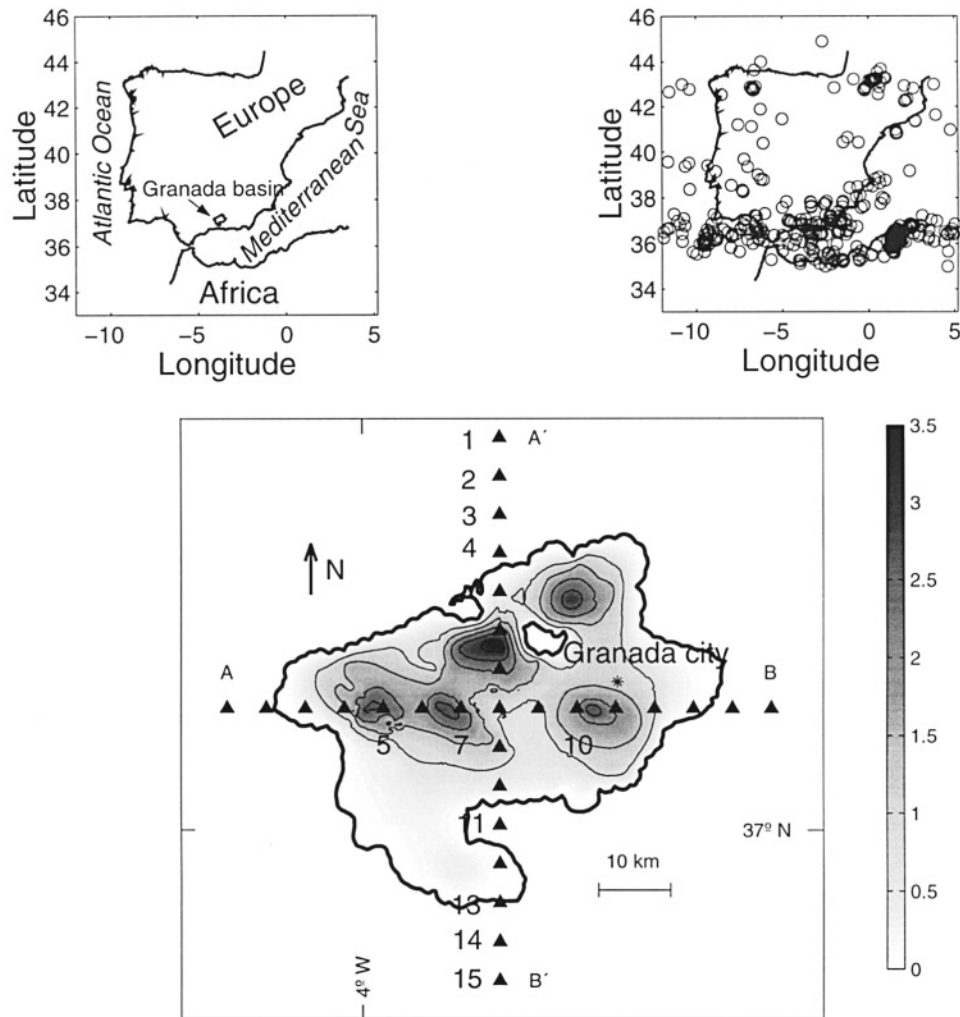


Figure 1. (Upper left): Map showing the location of the Granada Basin (Upper right): Map showing the epicenters (circles) of the region for earthquakes with magnitudes ≥ 4 in the period 1970–2001. (Bottom): Depth to the basement of the Granada Basin, with the locations of receivers in the profiles A–B and A'–B'. The contours have an interval of 600 m; darker shading indicates greater depth of the sediment–basement boundary. The units of the depth scale bar are in km.

the epicenters of the region for earthquakes with magnitudes ≥ 4 from the year 1970 to 2001 are presented in Fig. 1. Large amplifications that can be attributed to site effects have been observed in the basin (Morales, 1991). To analyze the response of the deep basement structure, we studied the amplification patterns and the snapshots of particle displacements in the free surface of a model of the Granada Basin. We also use profiles A–B and A'–B' (Fig. 1) to illustrate part of the effects of the sedimentary basin by means of synthetic seismograms and their corresponding polarigrams. The bulk of southern Spain's seismicity comes from the intercontinental collision of Africa and Eurasia; thus, an elevated number of earthquakes are produced south of the Granada Basin. Therefore, we use incident *P* and *S* waves coming from the south as the source input to the basin for the work presented here.

The Granada Basin

The Granada Basin is located in the southeast of Spain, in the central sector of the Betic Cordilleras mountain range. It is one of the larger intramountain Neogene–Quaternary basins of the Betic ranges. Geologically, the Granada Basin is bounded to the north and to the west by sub-Betic domain materials, mainly Jurassic and Cretaceous carbonate sedimentary series belonging to the Sub-Iberic paleomargin, and to the south and east by Alpujarrides metamorphic units (schists, phyllites, and quartzites of Palaeozoic and Triassic age and marbles of the Triassic period) of the Alborán domain (García Dueñas and Balanyá, 1986). The geologic evolution of this big basin has been the subject of previous studies (see, e.g., García Dueñas and Balanyá, 1986; Rodríguez Fernández *et al.*, 1989; Morales *et al.*, 1990; Sanz de Galdeano and Vera, 1992; Reicherter, 2001).

Southern Spain has the highest seismic hazard in the Iberian Peninsula, as shown in the maximum horizontal acceleration map for a return period of 500 years (Norma de Construcción Sismoresistente NCSE-94, 1995). The contribution of seismicity to the hazard is a consequence of the lithosphere collision between the Euroasiatic and African plates on a regional scale. The Granada Basin has the highest level of microseismic activity (magnitude <3.5) in the Iberian Peninsula (De Miguel *et al.*, 1989). Most of the seismic energy is released by earthquakes with magnitudes <5.0 ; however, catastrophic earthquakes have occurred in the past. In fact, the destructive Andalusian earthquake of 25 December 1884 ($I_0 = X$) occurred near Alhama de Granada, located in the south of the Granada Basin, producing great damage throughout the region (Vidal, 1986). Furthermore, J. M. Ibáñez *et al.* (unpublished results, 2001) estimated a maximum intensity–magnitude relationship for historical earthquakes in the south of Spain and found great magnitudes of ~ 6.5 – 7.0 inside the Granada Basin (e.g., the Andalusian earthquake of 25 December 1884 with M_{Imax} 6.8; the Granada earthquake in June 1431, with M_{Imax} 6.5), and outside of it (e.g., the Baza earthquake of 3 September 1531 with M_{Imax} 6.5 located ~ 80 km northeast of Granada city; the Almería earthquake of 22 September 1522 with M_{Imax} 6.8, located 100 km southeast of Granada city; the Málaga earthquake of January 1494 with M_{Imax} 6.5 located ~ 100 km southwest of Granada city).

The 3D basement structure of the Granada Basin was established by Morales *et al.* (1990) by means of an analysis and interpretation of gravity and seismic-reflection data. In this basin (see Fig. 1), there are important depocenters with depths >3000 m. The characteristic surficial dimensions of the sedimentary deposits are ~ 60 km \times 45 km. From the point of view of seismic hazard, local effects in the Granada Basin have been studied by using microtremors (Morales *et al.*, 1993), and coda and Lg waves (Ibáñez *et al.*, 1991). Moreover, Morales *et al.* (1996) used one small event, with magnitude M_w 5, as an empirical Green's function to obtain the synthetic records of a possible magnitude M_w 7.0 earthquake at various locations in the basin. The effect of the geological site conditions was reflected in the synthesized seismograms in which the peak ground acceleration reached values of ~ 250 cm/sec². The $S_{a_{\text{max}}}$ of the simulated seismograms, $\sim 0.8g$, also pointed out the importance of site effects in the Granada Basin in the ground motion induced by moderate earthquakes.

Velocity and density 1D profiles for various zones of the Granada Basin were derived by Kagawa *et al.* (1996), using the vertical-component records from a seismometer array and the dispersion characteristics of Rayleigh waves from microtremors as proposed by Horike (1985). In our computations, we use the properties calculated by Kagawa *et al.* (1996), in which the bedrock has a mass density of 2.7 g/cm³ and velocities of 5 and 3.2 km/sec for P and S waves, respectively. Although there is a thick, irregular surface layer with S -wave velocities as low as 516 m/sec, we assume

homogeneous basin sediments with mean values for the elastic properties because we are interested, in principle, in the seismic response of the deep structure of the sediments. Therefore, we set the values of 2.2 g/cm³ for mass density and 3.1 and 1.6 km/sec for P and S -wave velocities, respectively, inside the basin. To account for inelastic attenuation, we have assumed quality factors (Q) without depth or frequency dependence of 150 for both P and S waves in bedrock and of 100 for both waves inside the basin. These values have been assumed, based on the models of Q for S waves at depth proposed for southern Spain by Canas *et al.* (1988), who used a generalized inversion technique applied to the attenuation of Rayleigh waves.

Method and Discretization

We use the indirect boundary element method (IBEM) to compute the seismic response of the deep structure of the Granada Basin. In the IBEM, which is based on the so-called single-layer-boundary integral representation of displacements and tractions, the problems of diffraction and refraction of elastic waves are formulated in terms of boundary force densities. The boundary conditions of continuity of displacements and tractions between regions and those of null tractions at free surfaces, once discretized, lead to a system of linear equations in which the unknowns are the force densities of the boundary sources. Therefore, the method can be regarded as a numerical realization of Huygens' principle, in which the secondary sources are located on the surface boundaries. Details on this technique, in which the discretization of surfaces is achieved using circular elements and its implementation, can be found in Sánchez-Sesma and Luzón (1995).

Sánchez-Sesma and Luzón (1995) presented various examples of using the IBEM and solving the linear system of equations with the classic LU decomposition (see, e.g., Press *et al.*, 1992). However, in dealing with larger, more realistic 3D problems, some additional difficulties arise. In these calculations, to keep a reasonable ratio between the minimum wavelength and size of elements, the dimension of the coefficient matrix grows approximately with the square of frequency, and therefore the computational requirements can be too large for problems of practical interest. In a recent article, Ortiz-Alemán *et al.* (1998) overcame the problem by using threshold criteria to convert the full matrix into a sparse one and then using the biconjugate gradient method together with an iterative scheme to solve the linear system of equations. To test their approach, they satisfactorily reproduced the results of Luzón *et al.* (1997), who studied the diffraction of P , S , and Rayleigh waves by 3D topographic surfaces. On the other hand, use of the analytic Green's functions of a homogeneous full space, as is done in this work, implicitly limits the technique when the response for higher frequencies is wanted in a 3D layered basin. Nevertheless, with this technique and with the appropriate Green's functions, it is still possible, for example, to take into account a

layered structure or a medium with a velocity gradient, as has been done by F. Luzón *et al.* (unpublished results, 2001) in alluvial basins with 2D geometry with a vertical gradient of velocity.

In this work, we chose to deal with the linear system of equations obtained in the IBEM somewhat differently. We use a partitioned matrix instead of the full matrix, as did Sánchez-Sesma and Luzón (1995). We reordered rows and columns of the matrix to have block matrices and found that the system has a particular structure that can be easily constructed as

$$\begin{bmatrix} \mathbf{T}_{M_E M_E} & \mathbf{T}_{M_E L_E} & \mathbf{0}_{M_E L_R} & \mathbf{0}_{M_E K_R} \\ \mathbf{T}_{L_E M_E} & \mathbf{T}_{L_E L_E} & \mathbf{T}_{L_E L_R} & \mathbf{T}_{L_E K_R} \\ \mathbf{G}_{L_R M_E} & \mathbf{G}_{L_R L_E} & \mathbf{G}_{L_R L_R} & \mathbf{G}_{L_R K_R} \\ \mathbf{0}_{K_R M_E} & \mathbf{0}_{K_R L_E} & \mathbf{T}_{K_R L_R} & \mathbf{T}_{K_R K_R} \end{bmatrix} \begin{Bmatrix} \varphi_{M_E} \\ \varphi_{L_E} \\ \varphi_{L_R} \\ \varphi_{K_R} \end{Bmatrix} = \begin{Bmatrix} \mathbf{0}_{M_E} \\ -\mathbf{t}_{L_E} \\ -\mathbf{u}_{L_R} \\ \mathbf{0}_{K_R} \end{Bmatrix} \quad (1)$$

in which each term in the expression represents a submatrix block or a subvector. The submatrix $\mathbf{T}_{I_A J_B}$ and $\mathbf{G}_{I_A J_B}$ are related with the traction and displacement Green's functions, respectively, where I and J can be M (number of elements in the free surface of the half-space E), L (number of elements at the shared interface between the half-space E and inclusion R), or K (number of elements in the free surface of the inclusion R), and in which A and B refer to the domains E or R . The subvectors \mathbf{t}_{I_A} and \mathbf{u}_{I_A} are the tractions and displacements due to the free field, that is, those produced by the wave field in the absence of any irregularity, which includes incident and reflected waves by the half-space free surface. The blocks $\mathbf{0}_{M_E L_R}$, $\mathbf{0}_{M_E K_R}$, $\mathbf{0}_{K_R M_E}$, and $\mathbf{0}_{K_R L_E}$ are zero blocks, and subvectors $\mathbf{0}_{M_E}$ and $\mathbf{0}_{K_R}$ are zero vectors. It is easy to see that when applying the matrix static condensation approach, the linear system of equations displayed previously becomes several small linear systems of equations that can be solved using less memory than the original system. By taking out the zero blocks from the computations, the final solution spends a minor time but preserves the same accuracy as the formulation applied by Sánchez-Sesma and Luzón (1995). The static condensation approach is based on an implicit factorization of the coefficient matrix by taking advantage of the location of the zero blocks near the upper right and lower-left corners of the system. Considering the first and fourth block rows of the system, we can write

$$[\mathbf{T}_{M_E M_E}][\mathbf{P}_1] = [\mathbf{T}_{M_E L_E}] \quad (2)$$

$$[\mathbf{T}_{K_R K_R}][\mathbf{P}_2] = [\mathbf{T}_{K_R L_R}] \quad (3)$$

where $[\mathbf{P}_1]$ and $[\mathbf{P}_2]$ are unknown intermediate matrices that can be solved as a set of simultaneous equations. Then,

$$\begin{aligned} [\mathbf{Q}_{11}] &= [\mathbf{T}_{L_E L_E}] - [\mathbf{P}_1][\mathbf{T}_{L_E M_E}] \\ [\mathbf{Q}_{12}] &= [\mathbf{T}_{L_E L_R}] - [\mathbf{P}_2][\mathbf{T}_{L_E K_R}] \\ [\mathbf{Q}_{21}] &= [\mathbf{G}_{L_R L_E}] - [\mathbf{P}_1][\mathbf{G}_{L_R M_E}] \\ [\mathbf{Q}_{22}] &= [\mathbf{G}_{L_R L_R}] - [\mathbf{P}_2][\mathbf{G}_{L_R K_R}] \end{aligned} \quad (4)$$

where $[\mathbf{Q}_{11}]$, $[\mathbf{Q}_{12}]$, $[\mathbf{Q}_{21}]$, and $[\mathbf{Q}_{22}]$ are intermediate matrices that can be easily computed and yield a new compact system of linear equations at one fourth the size of the original system, which can be expressed as follows:

$$\begin{bmatrix} \mathbf{Q}_{11} & \mathbf{Q}_{12} \\ \mathbf{Q}_{21} & \mathbf{Q}_{22} \end{bmatrix} \begin{Bmatrix} \varphi_{L_E} \\ \varphi_{L_R} \end{Bmatrix} = \begin{Bmatrix} -\mathbf{t}_{L_E} \\ -\mathbf{u}_{L_R} \end{Bmatrix} \quad (5)$$

After solving this system, φ_{L_E} and φ_{L_R} are known force density vectors. So, the final step in the algorithm consists in the computation of the only unknown force density vectors, φ_{M_E} and φ_{K_R} , as follows:

$$\begin{aligned} \{\varphi_{M_E}\} &= -[\mathbf{P}_1]\{\varphi_{L_E}\} \\ \{\varphi_{K_R}\} &= -[\mathbf{P}_2]\{\varphi_{L_R}\} \end{aligned} \quad (6)$$

In contrast to the threshold-biconjugate gradient approach by Ortiz-Alemán *et al.* (1998) that works well for a relatively low frequency, our scheme has no implicit truncation errors, and thus, it is stable at higher frequencies for both alluvial valleys and topographies. The computations are done in a very efficient computer program in FORTRAN 90 with dynamic memory that does not waste any extra resources. In this way, it is possible to compute, in the same computer and with the same 3D problem, the solution corresponding to approximately twice the frequency calculated with the classic form using the full matrix in the IBEM.

Moreover, we dynamically discretized all surfaces in the model. To do this, we computed a discrete grid for every frequency analyzed, in such a way that we always have at least 4.5 boundary elements per wavelength of S waves in each region. For the irregular surfaces, we constructed a grid formed by rectangular elements that cover the complete surface. After this, each planar rectangular element of the grid is assumed to be a circle with the same surface as that of the rectangular element. On the other hand, in the flat boundaries, that is, in the free surfaces of the half-space and the basin, the elements are distributed with constant distances from the origin of our local coordinate system, forming different adjacent rings. The total surface of a ring is equal to the sum of the surfaces of all of the elements of the ring. The flat free surface of the bedrock was discretized up to a radial distance of 55 km from the origin of our coordinate system, which is located at the common point that is shared by both profiles A–B and A'–B', in the centre of the basin. In Fig. 2, an example of the distribution of boundary elements of the basement can be seen for a frequency of 0.149 Hz.

Results

We used the IBEM in the frequency domain, and we have computed the basin's response for 77 frequencies from 0 up to 0.312 Hz, for incident P , SV , and SH plane waves propagating from the south. The frequency of 0 Hz corresponds to the case where no inclusion exists, that is, the solution of the half-space.

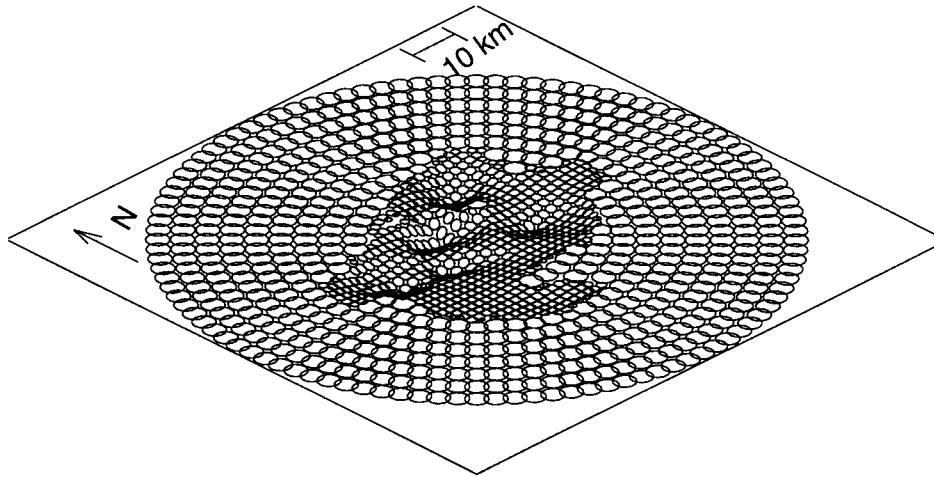


Figure 2. Example of discretization of the sediment–basement boundary for the frequency of 0.149 Hz.

The first results that we present show the influence of the deep structure of the Granada Basin on the amplification patterns for incident *SH* plane waves at various frequencies. We have selected incident angles of 0° and 60° with respect to the vertical. These results can be seen in Fig. 3 and 4, respectively, for the E–W (transverse motion), N–S (radial motion), and vertical components of displacement. For the sake of comparison, in both figures the amplification patterns are displayed at the same frequencies (0.149, 0.198, 0.248, and 0.312 Hz). We can clearly observe in both figures, even for relatively low frequencies, the amplifications produced by the deep structure of the Granada Basin. In fact, for the E–W component, the basin produces large amplifications for the chosen frequencies. In particular, for a vertical incidence (Fig. 3), the amplification reaches to nearly 10 times the amplitude of the incident source wave, in the frequency of 0.312 Hz, at various basin locations. For the same component of displacement outside the basin, the amplitude of the observed motion is about two times the incident one, as expected. For N–S and vertical motions, the amplification pattern is very interesting. Generally speaking, the maximum levels of the displacement are produced at those places where the depths of the basin are greater, that is to say, at the known depocenters. On the other hand, these maximum levels increase with frequency for both incidences, 0° and 60° . For both vertical incidence and the N–S component, the displacement amplitudes reach values larger than 5.

These effects, which cannot be obtained using 1D or 2D numerical modeling, correspond to the 3D nature of the deep basement of the Granada Basin. Fig. 5 shows the comparison of the 1D and 3D response for vertically incident *SH* waves at various receivers across the basin. The 1D solution corresponds to the model of a single layer over a half-space, with the same thickness as that of the depth of the basement at each station. The selected stations (5, 7, and 10) on profile A–B are next to the depocenters, with basement depths of 2295 m, 1908 m, and 1744 m, respectively. The 3D response

of the Granada Basin is more complex than the 1D, even at low frequency, as can be observed in Fig. 5. In the transverse displacement, the amplitude levels of the 1D and 3D responses at receivers 7 and 10 are quite similar, but on the other hand, the resonant frequency in the complete 3D solution at station 7 is slightly shifted to 0.2338 Hz. At station 5, the response is different in both the amplification level and the frequency content. In fact, the 1D solution predicts an amplification of 4.91 at a frequency of 0.1743 Hz, whereas the complete 3D response has an amplitude near 7 at 0.2480 Hz.

For the radial and vertical components, the response is completely different. Whereas the amplitudes in the 1D models are equal to zero in all cases, for the 3D case, these displacements are comparable to the amplitude of the incident wave only at lower frequencies. Moreover, in the radial motion at station 10, the 3D amplification is two times the incident one at frequencies near 0.3 Hz.

Analysis of Wave Propagation

In this section, we compute the seismic response in the time domain by using an incident Ricker wavelet (Ricker, 1977). In our computations, we used a characteristic period of $t_p = 6.5$ sec and a time lag of $t_s = 40$ sec. This pulse represents the input motion, which has a waveform that runs from $\mathbf{u}_{\min} = -0.4432$ to $\mathbf{u}_{\max} = 1$ displacement unit, as shown in Fig. 6. With the aim of studying the main characteristics of elastic wave propagation within our Granada Basin model, we use *P*- and *SV*-plane waves coming from the south, with an incident angle of 30° relative to the vertical.

In the case of the incident *P*-wave source, we computed the time response from the various frequencies studied by using Fourier synthesis. Approximately 18 sec of the radial (N–S) displacements are depicted in Fig. 7 by means of

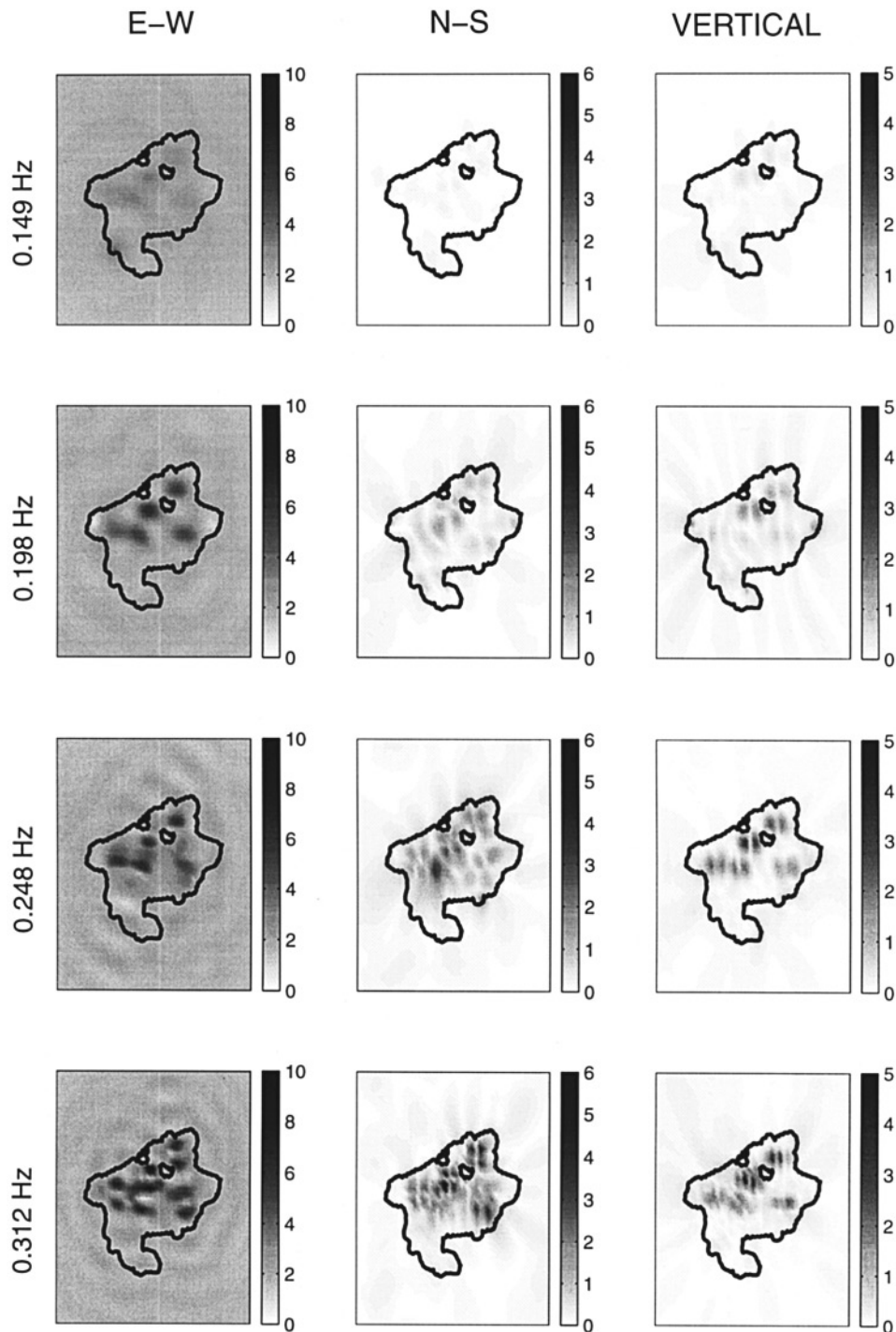


Figure 3. Amplifications, relative to the amplitude of the incident wave, of the three components of displacement at various frequencies in the Granada Basin for an *SH* wave coming from the south and with vertical incidence. The zero-depth contour of the basin is shown for reference.

snapshots at different times. Note that displacements observed at the free surface for this component are in the range from -1.8 to 2 displacement units, as shown on the scale bar, whereas the incident motion produced by the Ricker pulse in the N-S component ranges from $\mathbf{u}_{\min}(\text{N-S}) = \sin$

$30 \cdot \mathbf{u}_{\min} = -0.2216$ to $\mathbf{u}_{\max}(\text{N-S}) = \sin 30 \cdot \mathbf{u}_{\max} = 0.5$ displacement units, that is, in some times and positions, the amplification produced is ~ 8 . The *P* wave arrives after 36.8826 sec in the shallower part of basin to the south. These first displacements, represented with negative (dark shades)

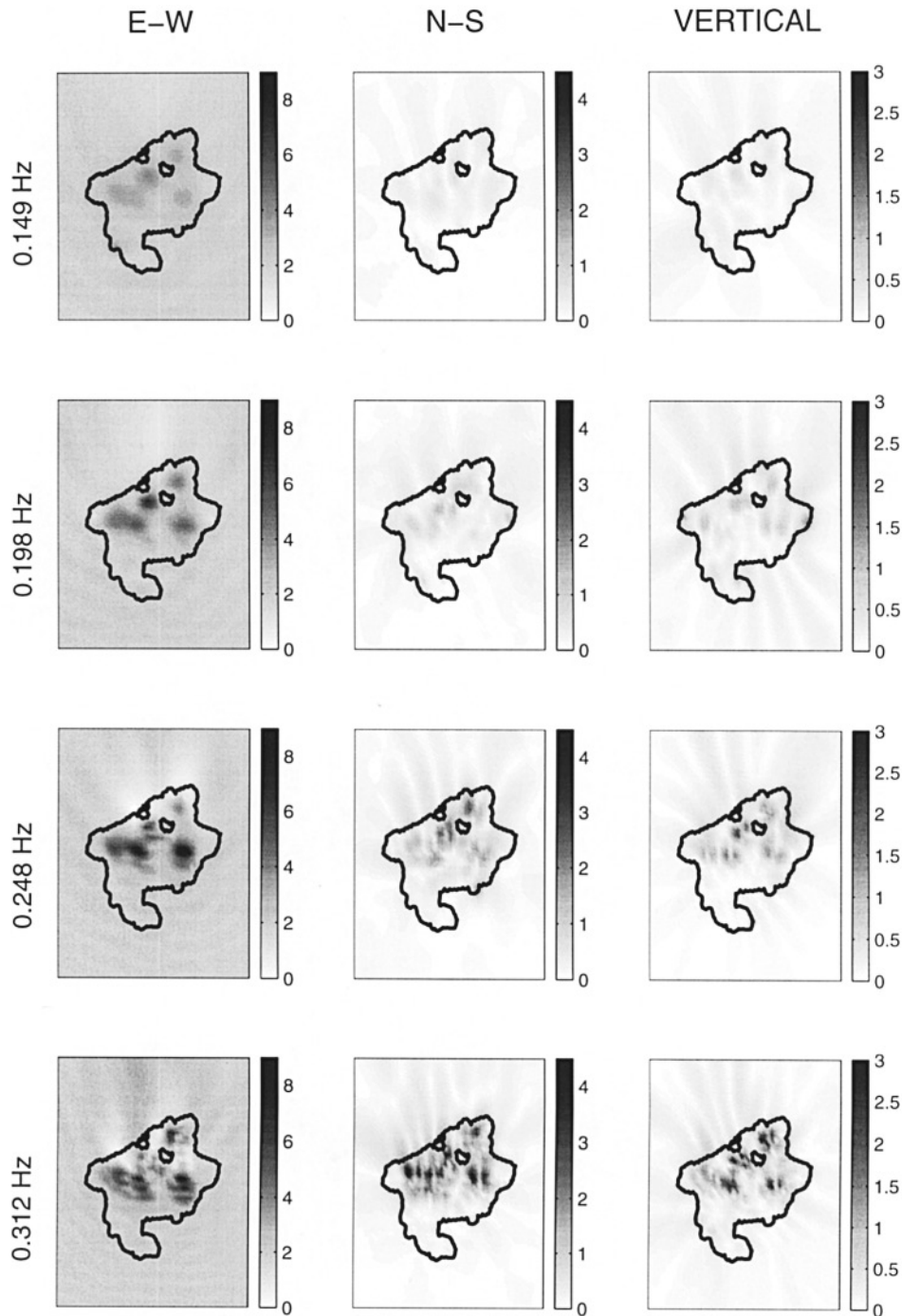


Figure 4. Same as Fig. 3, but for an *SH* wave coming from the south and with an incident angle of 60° with respect to the vertical.

amplitudes inside and outside the sediments, do not produce any remarkable effects. Nevertheless, after a time of 40.0898 sec, the direct wave begins to be amplified, as can be seen at this time (dark shades inside the basin) and in the following snapshot (light shades inside the basin). While the incident wave is traveling through the basin, the strongest ground motion is found at sites where the basin is deeper.

This effect is more prominent for the radial component than for the vertical one (not shown). After the direct wave departs from the northern part of the model ($t = 46.5041$ sec), the mechanical energy that remains trapped inside the basin continues producing displacements at the free surface. As before, the major displacements for $t > 46.5041$ sec are observed again at the locations above the deepest parts of the

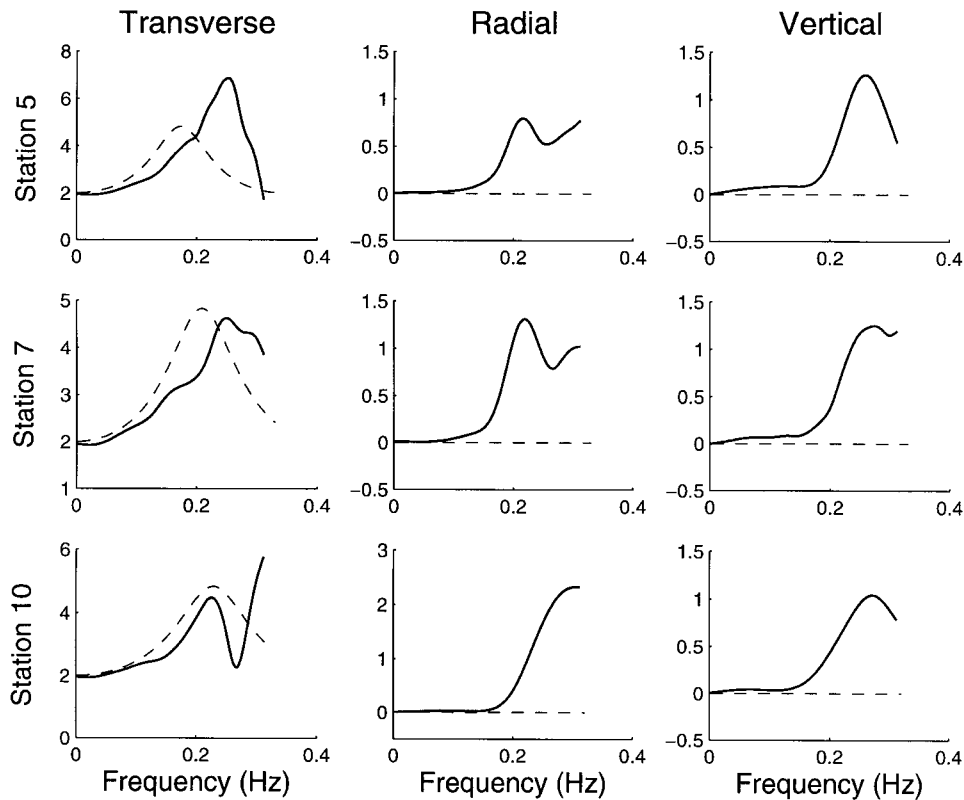


Figure 5. 1D (dashed line) and 3D (solid line) seismic responses for vertically incident *SH* waves at stations 5, 7, and 10 of the profile A–B shown in Fig. 1.

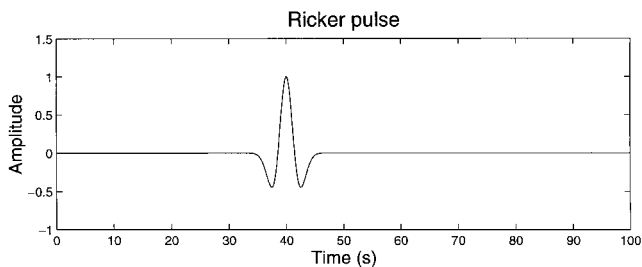


Figure 6. Incident Ricker pulse used in our study. The characteristic period is of $t_p = 6.5$ sec and the time lag, of $t_s = 40$ sec.

basin and are more significant on the N–S component presented in Fig. 7.

Results for the radial displacements produced by an incident *SV*-wave source are shown in Fig. 8. The snapshots are given for the same times used for the *P*-wave simulation. For this incident wave, the displacements observed at the free surface for the N–S component are in the range of -1.8 to 2.4 displacement units, whereas the incident motion in the N–S component ranges from $\mathbf{u}_{\min}(\text{N-S}) = \cos 30 \cdot \mathbf{u}_{\min} = -0.3838$ to $\mathbf{u}_{\max}(\text{N-S}) = \cos 30 \cdot \mathbf{u}_{\max} = 0.8660$ displacement units. The motion begins to be amplified inside the basin after 40.0898 sec, and the amplification is more important in the following times when the direct wave crosses

our model of the Granada Basin. This has been observed in both radial and vertical components. After this, the energy is trapped inside the structure, producing displacements that can be observed from $t = 46.5041$ sec and subsequent times, when the direct wave exits from the northern part of the basin.

A small quantity of energy is generated at the edges of the basin. This cannot be well observed in the snapshots of Fig. 8, because the amplitudes of these displacements are low in comparison with the motion produced by the incident wave field. This small quantity of energy can be better observed in Fig. 9, where we present the synthetic seismograms of vertical (*V*), radial (*R*), and tangential (*T*) components of displacement at the receivers along the profiles A–B and A'–B' of Fig. 1. The ground motion inside the sedimentary basin is generally more complex than observed in hard rock, as shown on the tangential component of both profiles where no direct wave exists. Comparing this component on both profiles, we see that the one corresponding to the profile A–B presents a more complicated pattern than the displacement of profile A'–B'. This is probably because profile A–B crosses various depocenters of the Granada Basin, whereas profile A'–B' crosses only one. Note also that there are more stations inside the basin on profile A–B. Nevertheless, the characteristics of the propagating phases within the basin, which can be seen on the tangential components, are differ-

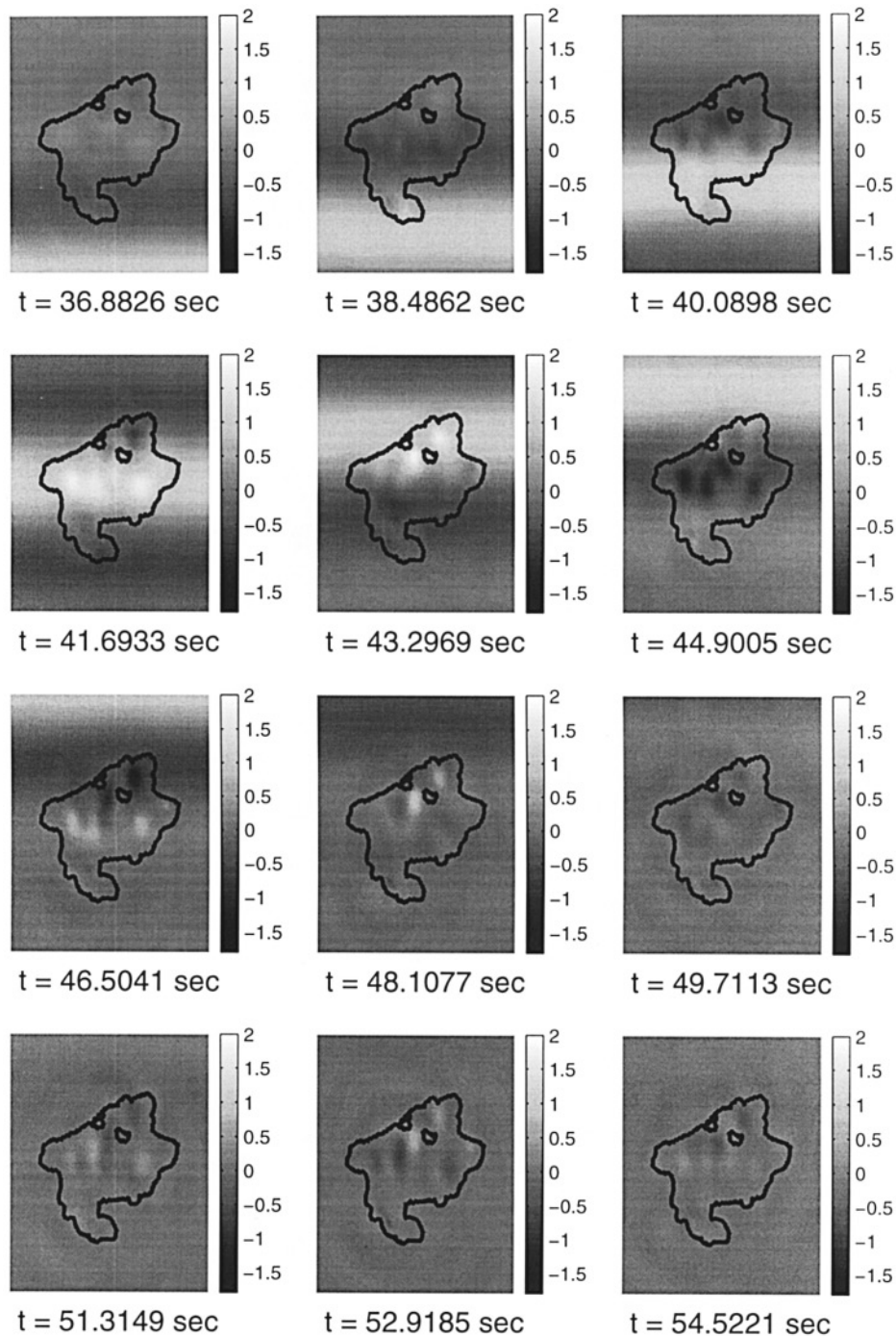


Figure 7. Radial (N-S) displacement snapshots of wave propagation in the Granada Basin for a simulation with a P wave propagating from the south and with an incident angle of 30° with respect to the vertical. Light (dark) shading depicts positive (negative) particle displacement. The zero-depth contour of the basin is shown for reference.

ent. Whereas on A–B the propagation of a phase identified as a Rayleigh wave is observed, the corresponding wave that travels on A'–B' can be identified as a Love wave. On the other hand, the emission of waves radiated outside the Granada Basin is observed as well on the vertical and radial components of the A'–B' profile. These waves propagate

with more energy on the forward direction (from south to north) of the incident body wave. These can be identified as Rayleigh waves by means of the results given in Fig. 10, where we present the polarigrams in the radial–vertical plane for the incidence SV waves at the 15 receivers on profile A'–B'. These polarigrams display the variation in the displace-

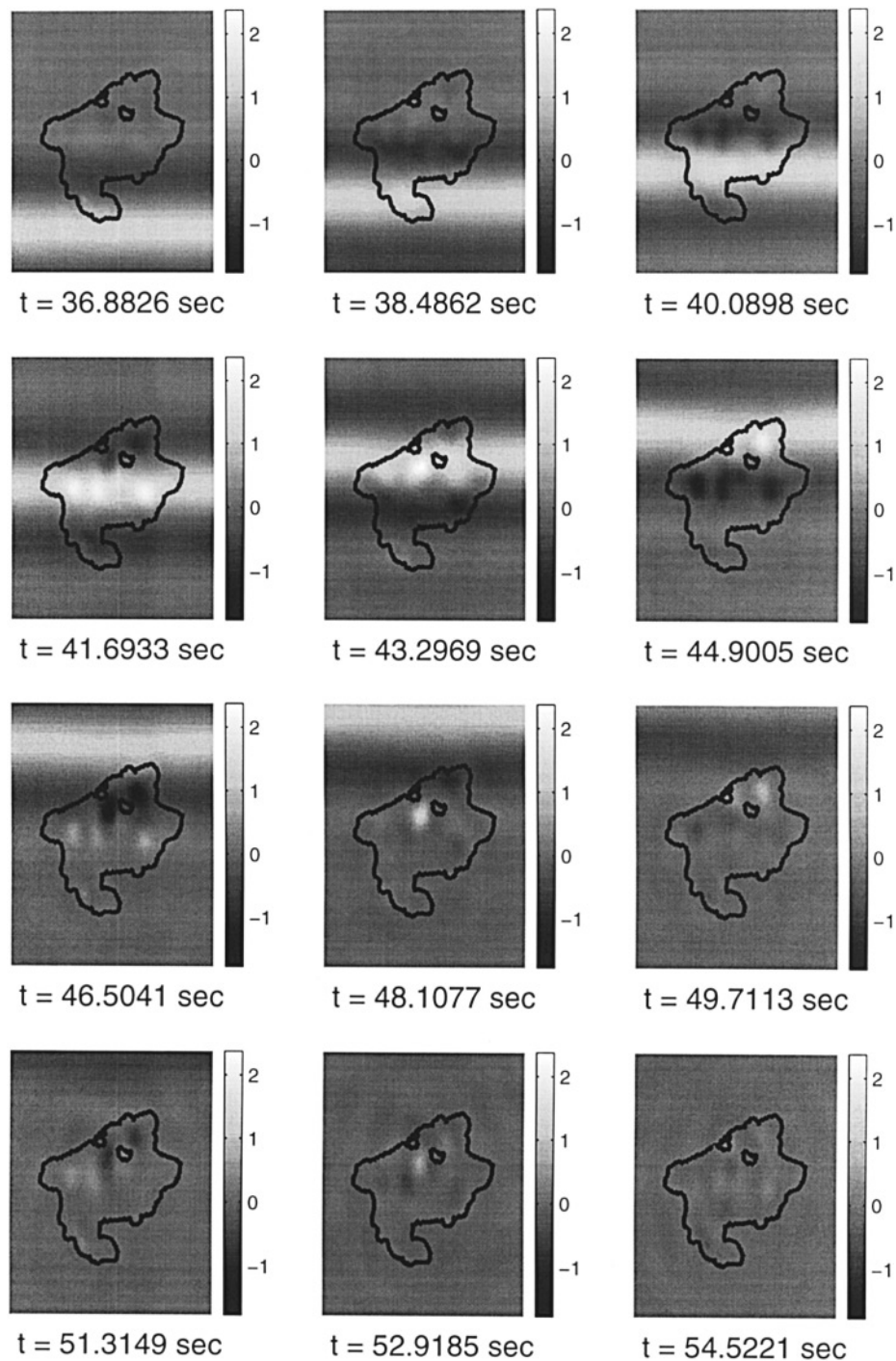


Figure 8. Same as Fig. 6, but for an incident *SV* wave.

ment vectors with time. The Rayleigh waves, showing little energy, can be identified in the later arrivals, with their characteristic elliptical and retrograde motion. This is the case not only for a half-space but also for the fundamental Rayleigh mode in a layer as well.

Part of the effects observed in the Granada Basin are consistent with those obtained by Olsen *et al.* (1995), who simulated the 3D wave propagation in the Salt Lake Basin

(Utah), and other aspects of our computations are similar to the results of Frankel (1993) from 3D finite-difference modeling of the San Bernardino valley (California). Whereas in the Salt Lake Basin the resonating energy is radiated into the bedrock surrounding the sediments without generating any well-developed, coherent surface waves or trapped body-wave phases in the basin, in the San Bernardino model, clear, large-amplitude surface waves were generated at the

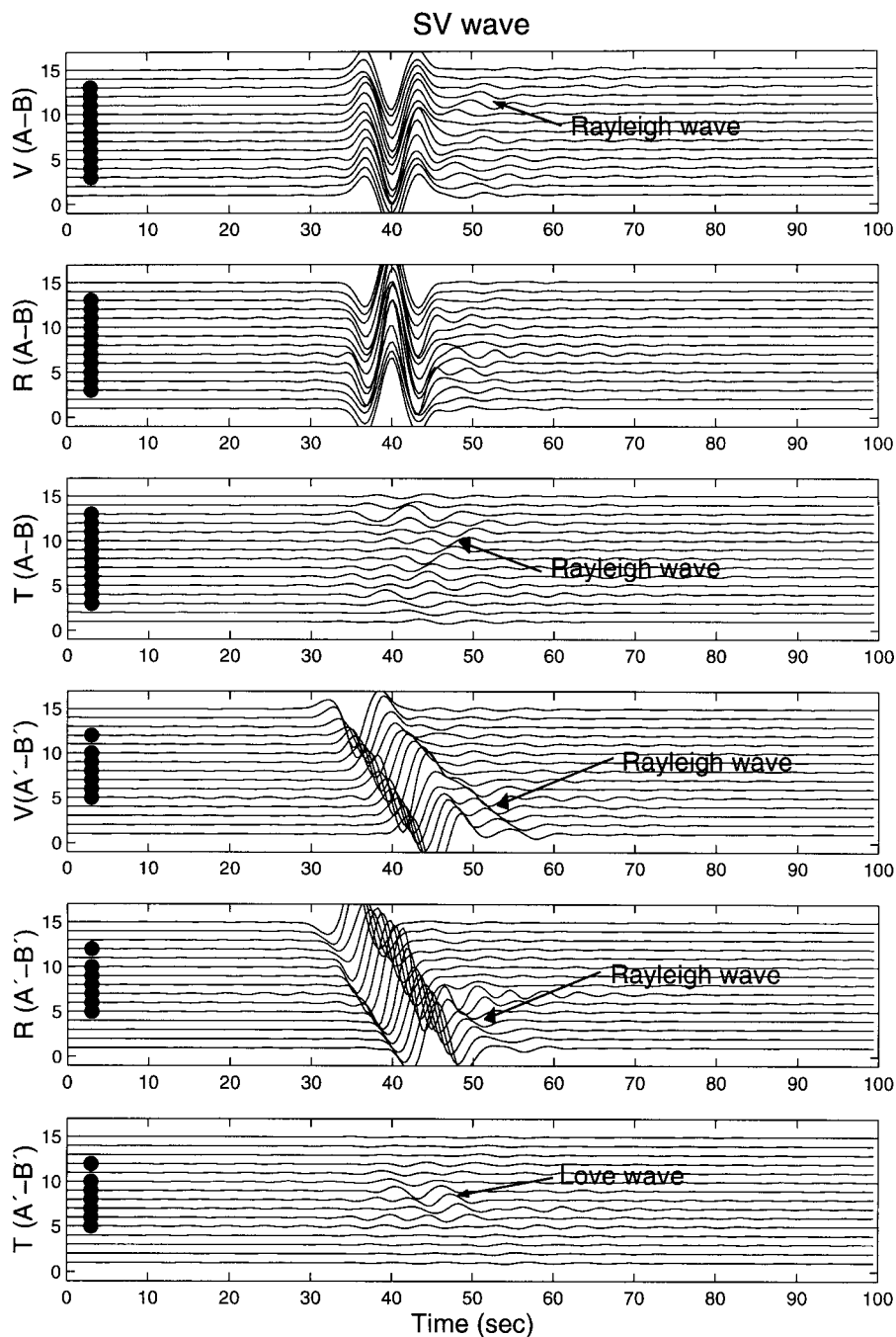


Figure 9. Seismograms of the vertical (V), radial (R), and tangential (T) components of displacement at the 15 receivers of the $A-B$ profile and the 15 receivers of the $A'-B'$ profile. The seismograms that have a solid circle are located inside the Granada Basin.

edges of the basin. The Granada Basin has an average behavior between these two models. In our computations, part of the energy observed after the incident wave, in the synthetic seismograms of the profiles $A-B$ and $A'-B'$, is not well developed, and although surface waves have been detected inside and outside the Granada Basin, these waves do not propagate with large amplitudes, as has occurred in the San Bernardino valley. This average behavior can be ex-

plained by various similitudes and differences among the three models: (1) The low-impedance contrast between the sediments and the bedrock in the Granada Basin (equal to 2.45) produces similar effects to those in the Salt Lake Basin (with impedance contrast equal to 2.69). In contrast, the impedance contrast in the San Bernardino Basin is higher (equal to 4.3). The effects produced by the impedance contrast are well known and have been defined. As has been

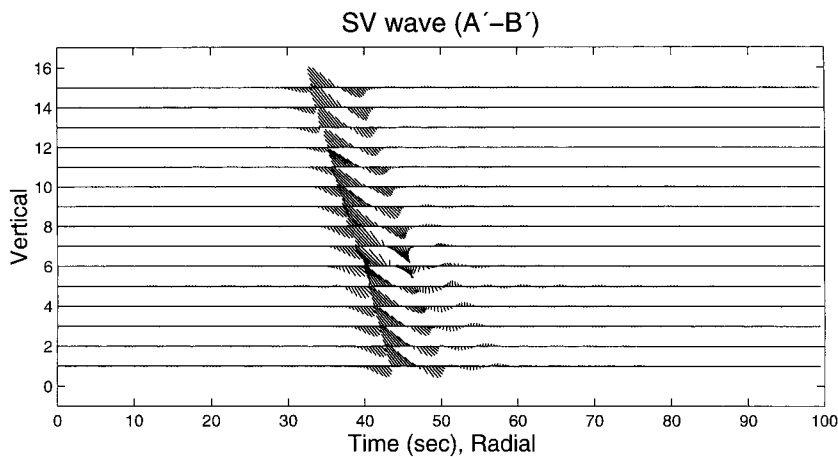


Figure 10. Polarigrams in the radial-vertical plane for the incidence of *SV* waves at the 15 receivers of the A'-B' profile.

pointed out by previous authors (see e.g., Bard and Bouchon, 1980; Sánchez-Sesma *et al.*, 1993), when high-impedance contrast exists, surface waves are very efficiently generated and reflected at the edges of the basin. (2) As was showed by Hill *et al.* (1990), energetic surface waves can be generated at steeper basin slopes as well. The Granada Basin has many zones where the slope of the basement is $\sim 30\%$, in particular the northern part, in which this type of wave can be generated. This is similar to the San Bernardino Basin, where exist slopes $\sim 30\%$ near the southern part of the San Jacinto fault. In contrast, the model of the Salt Lake Basin, which does not produce well-developed coherent surface waves, has slopes of $\sim 10\%$. (3) The incident wave field of the Granada Basin (plane waves) considered in this work is similar to that of Olsen *et al.* (1995), who used *P*-plane waves in the Salt Lake Basin. Conversely, Frankel (1993) used a kinematic time- and space-varying source function simulating an *M* 6.5 earthquake occurring on the edge of the basin. This author observed that the largest velocities in the San Bernardino Basin were dependent on the direction of rupture propagation of the seismic source and that maximum shaking was also dependent on asperity positions and radiation pattern.

Conclusions

We have computed the seismic response of the 3D basement structure of a model of the Granada Basin by using the IBEM for incident *P*- and *S*-plane waves. In this study, we have solved the linear system of equations by using a partition matrix method, which is different from the classic LU decomposition that has been used in previous articles. The advantage of the partition matrix method used here is that it is possible to calculate, on the same computer and with the same model configuration, the solution corresponding to approximately twice the frequency computed with the classic LU.

We have analyzed the results in both frequency and time domains, and for the range of frequencies that we have been able to compute, it has been observed that the most relevant

site effects are due to the local amplifications produced inside the sediments. For *SH* waves, the amplification factor reaches values near 10 times the amplitude of the incident wave for some specific frequencies and locations. In the other case, for the characteristic period considered in this work for the incident *P*-wave Ricker pulse, the amplification arrives at some specific times and positions around 8. In general, for the incident plane waves considered in this work, the amplification levels are not too large, because the impedance contrast between the sediments and the bedrock (equal to 2.45) is relatively low.

The geometry of the basin contributes in a deterministic way to the response. Where basement depths are >3 km, we see a characteristic seismic response in the range of frequencies dealt with in this study that cannot be predicted using a 1D model. The amplification patterns of the displacement observed for incident *P*, *SV*, and *SH* waves have maximum levels at those locations where the depths of the basin are larger. Moreover, according to our model, the Granada Basin is likely to produce and emit surface waves with little energy, as we observed in the synthetic seismograms and their corresponding polarigrams. These waves in this basin do not cause large displacements. The generation of these surface waves is a common feature that has been observed in many basins around the world by using real records and that have been reproduced using numerical methods for modeling of the seismic response of similar geological structures (see, e.g., Hatayama and Fujiwara, 1998).

One of the more important conclusions that we can obtain from this work is that a simple 3D model allows us to point out important site effects that may influence the seismic motion at future earthquakes in the Granada Basin between 0 and 0.312 Hz. Therefore, it is necessary to allocate resources and effort in three directions: (1) setting an adequate accelerograph array to cover the basin in an efficient way, particularly in those places where we have observed the major amplifications in this study; (2) the development of specific and controlled experiments to improve the basin's model to obtain the complete geometry and physical properties of the different sediments that fill the basin; and

(3) the consideration of more realistic aspects into numerical modeling, such as the sedimentary layering, to obtain the seismic response of the Granada Basin for higher frequencies, or the use of nearby sources, which can change the response because of the direction of rupture propagation or the radiation pattern, as was shown by Frankel (1993) in the San Bernardino Basin. With the IBEM and the appropriate Green's functions, it is possible to take into account a layered structure or a medium with a velocity gradient, as was done by Luzón *et al.* (unpublished results, 2001) in 2D alluvial basins with a vertical gradient of velocity. On the other hand, the inclusion of near sources can be performed by constructing the kinematic model of a finite fault with a set of point sources with their appropriate rupture velocity. Each of these point sources can be constructed with the corresponding Green's functions, as was done by Luzón *et al.* (1999), who computed the displacements produced by near seismic point sources to 3D mountains with the IBEM. All of this could provide us with good estimations of seismic motion with which to compare the records of ground acceleration, with the aim of understanding the complex seismic response of the Granada Basin.

Acknowledgments

We thank W. J. Stephenson and T. Kagawa for their helpful suggestions and reviews of the manuscript. Thanks are given to Z. al Yuncha for his help in the digitization of part of the Granada Basin. This work was performed during the visit of S. A. Gil-Zepeda to the University of Almería, Spain. Part of the computations were done with the computers of the DMPN Institute de Physique du Globe de Paris, France; the kindness of Prof. Jean-Pierre Vilotte is greatly appreciated. This work was partially supported by CICYT, Spain, under Grants AMB99-1015-CO2-02 and AMB99-0795-CO2-01; by DGAPA-UNAM, Mexico, under Project IN104998; and by the research teams RNM-194 and RNM-103 of Junta de Andalucía, Spain.

References

- Aki, K. (1988). Local site effects on strong ground motion, in *Earthquake Engineering and Soil Dynamics II—Recent Advances in Ground Motion Evaluation*, J. Lawrence Von Thun (editor), American Society of Civil Engineering, New York, 103–155.
- Bard, P.-Y., and M. Bouchon (1980). The seismic response of sediment-filled valleys, part 1: the case of incident SH waves, *Bull. Seism. Soc. Am.* **70**, 4, 1263–1286.
- Canas, J. A., F. De Miguel, F. Vidal, and G. Alguacil (1988). Anelastic Rayleigh wave attenuation in the Iberian Peninsula, *Geophys. J. Int.* **95**, 391–396.
- De Miguel, F., F. Vidal, G. Alguacil, and J. M. Guirao (1989). Spatial and energetics trends of the microearthquakes activity in the central Betics, *Geodin Acta*, **3**, 87–94.
- Frankel, A. (1993). Three-dimensional simulations of ground motions in the San Bernardino Valley, California, for hypothetical earthquakes on the San Andreas fault, *Bull. Seism. Soc. Am.* **83**, 1020–1041.
- Frankel, A., and W. Stephenson (2000). Three-dimensional simulations of ground motions in the Seattle region for earthquakes in the Seattle fault zone, *Bull. Seism. Soc. Am.* **90**, 1251–1262.
- García Dueñas, V., and J. C. Balanyá (1986). Estructura y naturaleza del arco de Gibraltar. *Maleo-Bol. Inf. Soc. Geol.* **2**, 23 (in Spanish).
- Hatayama, K., and H. Fujiwara (1998). Excitation of secondary Love and Rayleigh waves in a three-dimensional sedimentary basin evaluated by the direct boundary element method with normal modes, *Geophys. J. Int.* **133**, 260–278.
- Hill, J., H. Benz, M. Murphy, and G. T. Schuster (1990). Propagation and resonance of SH waves in the Salt Lake Valley, Utah. *Bull. Seism. Soc. Am.* **80**, 23–42.
- Horike, M. (1985). Inversion of phase velocity of long-period microtremors to the S-wave-velocity structure sown to the basement in urbanized areas, *J. Phys. Earth* **33**, 59–96.
- Ibáñez, J., J. Morales, F. De Miguel, F. Vidal, G. Alguacil, and A. Posadas (1991). Effect of a sedimentary basin on estimations of Q_c and Q_{Lg} . *Phys. Earth Planet. Interiors* **66**, 244–252.
- Kagawa, T., and Group for Spanish-Japanese joint work on microzonation of Granada basin (1996). Microtremor array observation in the Granada basin, southern Spain, in *Homenaje en Honor del Profesor Fernando de Miguel Martínez*. F. Vidal, M. Espinay J. A. Esquivel (Editors), Universidad de Granada, Granada, Spain, 287–304 (in Spanish).
- Luzón, F., F. J. Sánchez-Sesma, J. L. Rodríguez-Zúñiga, A. M. Posadas, J. M. García, J. Martín, M. D. Romacho, and M. Navarro (1997). Diffraction of P, S and Rayleigh waves by three-dimensional topographies, *Geophys. J. Int.* **129**, 571–578.
- Luzón, F., F. J. Sánchez-Sesma, A. Gil, A. Posadas, and M. Navarro (1999). Seismic response of 3D topographical irregularities under incoming elastic waves from point sources, *Phys. Chem. Earth (A)*, **24**, 231–234.
- Morales, J. (1991). Caracterización de la respuesta sísmica local en las cuencas de Granada (España) y Ciudad Guzmán (México) mediante el análisis espectral de microterremotos y terremotos. *Ph.D. Thesis*. University of Granada, Spain, 276 Pp (in Spanish).
- Morales, J., F. Vidal, F. De Miguel, G. Alguacil, A. Posadas, J. Ibáñez, J. M. Guzmán, and J. M. Guirao (1990). Basement structure of the Granada basin, Betic Cordilleras, southern Spain, *Tectonophysics* **177**, 337–348.
- Morales, J., K. Seo, T. Samano, J. A. Peña, J. Ibáñez, and F. Vidal (1993). Site response on seismic motion in the Granada basin (southern Spain) based on microtremor measurement, *J. Phys. Earth* **41**, 221–238.
- Morales, J., S. K. Singh, and M. Ordaz (1996). Analysis of Granada, Spain earthquake of 24 June, 1984 ($M = 5$) with emphasis on seismic hazard in the Granada basin, *Tectonophysics* **257**, 253–263.
- Norma de Construcción Sismorresistente NCSE-94, (1995). Boletín Oficial del Estado, February 8. Ministerio Obras Públicas, Transportes y Medio Ambiente, 3935–3980 (in Spanish).
- Olsen, K. B. (2000). Site amplification in the Los Angeles basin from three-dimensional modeling of ground motion. *Bull. Seism. Soc. Am.* **90**, 6B, S77–S94.
- Olsen, K. B., and R. J. Archuleta (1996). Three-dimensional simulation of earthquakes on the Los Angeles fault system. *Bull. Seism. Soc. Am.* **86**, 575–596.
- Olsen, K. B., J. C. Pechmann, and G. T. Schuster (1995). Simulation of 3D elastic wave propagation in the Salt Lake basin. *Bull. Seism. Soc. Am.* **85**, 1688–1710.
- Ortiz-Alemán, C., F. J. Sánchez-Sesma, J. L. Rodríguez-Zúñiga, and F. Luzón (1998). Computing topographical 3D site effects using a fast IBEM/conjugate gradient approach, *Bull. Seism. Soc. Am.* **88**, 393–399.
- Press, W. H., S. A. Teukolsky, W. T. Vetterling, and B. P. Flannery (1992). *Numerical Recipes in Fortran*, Cambridge University Press.
- Reicherter, K. R. (2001). Paleoseismologic advances in the Granada basin (Betic cordilleras, southern Spain). *Acta Geol. Hisp.* **36**, 278–281.
- Ricker, N. H. (1977). *Transient Waves in Visco-Elastic Media*, Elsevier, Amsterdam, Holland.
- Rodríguez Fernández, C., C. Sanz de Galdeano, and J. Fernández (1989). Genesis and evolution of the Granada Basin (Betic Cordillera, Spain). *International Symposium on Intermontane Basins, Geology & Resources*, Chiang Mai, Thailand, 294–305.
- Sánchez-Sesma, F. J. (1996). Strong ground motion and site effects, in *Computer Analysis of Earthquake Resistant Structures*, D. E. Beskos

- and S. A. Anagnostopoulos (editors), *Comp. Mech. Publications*, Southampton, 200–229.
- Sánchez-Sesma, F. J., and F. Luzón (1995). Seismic response of three dimensional alluvial valleys for incident *P*, *S* and Rayleigh waves, *Bull. Seism. Soc. Am.* **85**, 269–284.
- Sánchez-Sesma, F. J., J. Ramos-Martínez, and M. Campillo (1993). An indirect boundary element method applied to simulate the seismic response of alluvial valleys for incident *P*, *S* and Rayleigh Waves, *Earthquake Eng. Struct. Dyn.* **422**, 279–295.
- Sanz de Galdeano, C., and J. A. Vera (1992). Stratigraphic record and paleogeographical context of the Neogene basins in the Betic Cordillera, Spain, *Basin Res.* **4**, 21–36.
- Vidal, F. (1986). Sismotectónica de la región Béticas-Mar de Alborán, *Ph.D. Thesis*, University of Granada, Spain, 450 Pp (in Spanish).

Departamento de Física Aplicada
 Universidad de Almería
 Cañada de San Urbano
 s/n 04120 Almería, Spain
 (F.L.)

Instituto Andaluz de Geofísica y Prevención de Desastres Sísmicos
 Universidad de Granada
 Campus Universitario de Cartuja
 s/n 18071 Granada, Spain
 (F.L., J.M.)

Instituto de Ingeniería, UNAM
 Cd. Universitaria, Apdo. 70-472
 Coyoacán
 04510 México D.F., México
 (S.A.G.-Z., J.A., F.J.S.-S.)

Instituto Mexicano del Petróleo
 Eje Central 152
 07730, México D.F., México
 (C.O.-A)

Manuscript received 12 October 2001.